Electronic structure and *p*-type conduction mechanism of spinel cobaltite oxide thin films

X. C. Huang,[1,2] J. Y. Zhang,[1,2] M. Wu,[3] S. Zhang,[4] H. Y. Xiao,[4] W. Q. Han,[2] T.-L. Lee,[5] A. Tadich,[6,7] D.-C. Qi,[7,8] L. Qiao,[4,*] L. Chen,[2,†] and K. H. L. Zhang[1,‡]

[1]*State Key Laboratory of Physical Chemistry of Solid Surfaces, College of Chemistry and Chemical Engineering, Xiamen University, Xiamen 361005, People's Republic of China*

[2]*Department of Physics, Southern University of Science and Technology, Shenzhen, Guangdong 518055, China*

[3]*Department of Physics, Xiamen University, Xiamen 361005, China*

[4]*School of Physics, University of Electronic Science and Technology of China, Chengdu 610054, China*

[5]*Diamond Light Source Ltd., Harwell Science and Innovation Campus, Didcot, OX11 0DE, United Kingdom*

[6]*Australian Synchrotron, 800 Blackburn Road, Clayton, Victoria 3168, Australia*

[7]*Department of Chemistry and Physics, La Trobe University, Victoria 3086, Australia*

[8]*School of Chemistry, Physics and Mechanical Engineering, Queensland University of Technology, Brisbane, Queensland 4001, Australia*

(Received 5 May 2019; revised manuscript received 31 July 2019; published 3 September 2019)

This work reports a fundamental study on the electronic structure, optical properties, and defect chemistry of a series of Co-based spinel oxide (Co_3O_4, $ZnCo_2O_4$, and $CoAl_2O_4$) epitaxial thin films using x-ray photoemission and absorption spectroscopies, optical spectroscopy, transport measurements, and density functional theory. We demonstrate that $ZnCo_2O_4$ has a fundamental bandgap of 1.3 eV, much smaller than the generally accepted values, which range from 2.26 to 2.8 eV. The valence band edge mainly consists of occupied Co 3*d* t_{2g}^6 with some hybridization with O 2*p*/Zn 3*d*, and the conduction band edge of unoccupied e_g^* state. However, optical transition between the two band edges is dipole forbidden. Strong absorption occurs at photon energies above 2.6 eV, explaining the reasonable transparency of $ZnCo_2O_4$. A detailed defect chemistry study indicates that Zn vacancies formed at high oxygen pressure are the origin of a high *p*-type conductivity of $ZnCo_2O_4$, and the hole conduction mechanism is described by small-polaron hoping model. The high *p*-type conductivity, reasonable transparency, and large work function make $ZnCo_2O_4$ a desirable *p*-type transparent semiconductor for various optoelectronic applications. Using the same method, the bandgap of Co_3O_4 is further proved to be ∼0.8 eV arising from the tetrahedrally coordinated Co^{2+} cations. Our work advances the fundamental understanding of these materials and provides significant guidance for their use in catalysis, electronic, and solar applications.

DOI: 10.1103/PhysRevB.100.115301

I. INTRODUCTION

Cobalt-based spinel oxides (Co_3O_4, $ZnCo_2O_4$, $CoAl_2O_4$) exhibit intriguing physicochemical properties, demonstrating promising potential for renewable energy and electronics applications [1]. The electronic structure of these oxides is the critical factor in determining their physical and chemical properties. The parent compound Co_3O_4 crystallizes into a normal cubic spinel (AB_2O_4) structure (see Fig. 1), in which the tetrahedral *A* sites (T_d) are occupied by Co^{2+}, in a high spin state of $S = 3/2$, whereas the octahedral *B* sites (O_h) are filled with Co^{3+} in a low spin state, $S = 0$. Co_3O_4 exhibits superior catalytic activity for CO oxidation [2], methane combustion, and electrochemical water splitting [3,4], as well as excellent optoelectronic properties for use as a solar absorber material in photovoltaics because of its suitable bandgap for visible light absorption and as a *p*-type semiconductor channel for electronic devices [5,6]. Despite the wide technological applications, fundamental knowledge regarding the electronic structure and optical properties of Co_3O_4 remains very poorly understood, e.g., the values of the bandgap are still under debate and remains elusive [7]. Different bandgap values, including 2.2, 1.6, and 1.2 eV have been reported in literature for Co_3O_4 [8,9]. Recently, on the basis of near-infrared optical spectroscopy, Qiao *et al.* proposed that Co_3O_4 has a fundamental bandgap of 0.76 eV, almost 1 eV less than the generally accepted values [10]. They claim this gap is due to direct dipole-forbidden *d*-*d* transitions at T_d-site Co^{2+} cations. More interestingly, a long-lived decay (nanoseconds) of photoexcited carriers has been observed in Co_3O_4 in the near-infrared region, which is of particular interest in photovoltaic and photocatalytic devices [11].

Detailed knowledge of the electronic structures of Co-based spinel oxides is of crucial importance, because (i) it determines the optoelectronic properties; (ii) the bandgap value has been used as a benchmark for identifying appropriate Hubbard U values in density-functional theory (DFT+U) calculation of the catalytic behavior of Co_3O_4 [9,12,13]. For example, Selloni *et al.* have studied the structure and reactivity of Co_3O_4 (110) using DFT+U calculations, and showed that different U values resulted in quite significant differences in the calculated structural parameters, electronic properties, and surface energetics [14,15]. Similarly, Hu *et al.* showed

*liang.qiao@uestc.edu.cn
†chenlang@sustc.edu.cn
‡kelvinzhang@xmu.edu.cn

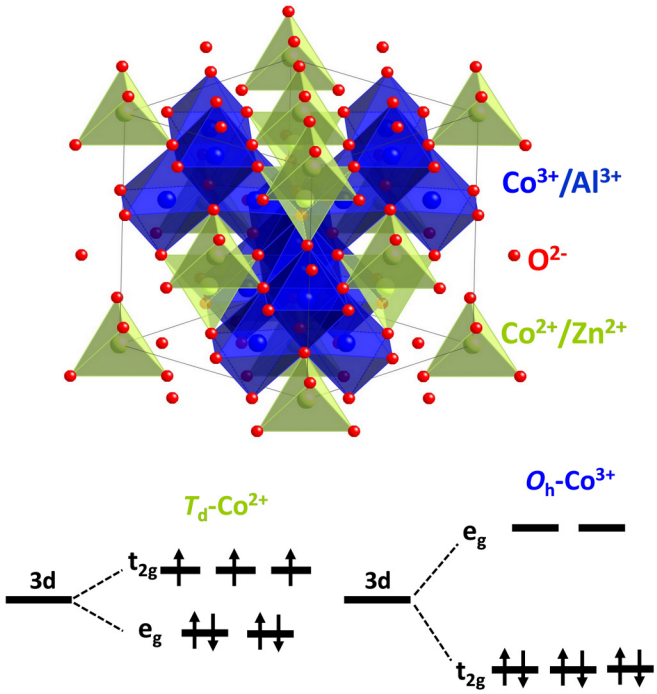

FIG. 1. Crystal structure of normal spinel, in which the tetrahedral sites (denoted as T_d) are occupied by divalent cations (Co^{2+} for Co_3O_4 and $CoAl_2O_4$; Zn^{2+} for $ZnCo_2O_4$) and the octahedral sites (O_h) are occupied by trivalent cations (Co^{3+} for Co_3O_4 and $ZnCo_2O_4$; Al^{3+} for $CoAl_2O_4$); bottom show the corresponding $3d$ electron states of the Co^{2+} in T_d, Co^{3+} ions in O_h crystal field.

that different U values can significantly influence the molecular adsorption energy, CO oxidation, and C−H activation of methane on Co_3O_4 surface [8]. Therefore, it is of great importance to gain an accurate description of the electronic structures and reliable U values to achieve the correct energy profile for reaction pathway in electrocatalysis [16].

$ZnCo_2O_4$, on the other hand, can be constructed from the substitution of the T_d site Co^{2+} in Co_3O_4 by Zn^{2+}, leaving the O_h Co^{3+} cations (Fig. 1). $ZnCo_2O_4$ has been attracting considerable research attention due to its applications in electrocatalysis, supercapacitors, and Li ion batteries [1]. More importantly, recent studies indicated that $ZnCo_2O_4$ is a promising wide bandgap *p*-type oxide, affording potential applications in transparent electronics, hole transport layers for photovoltaics, and ultraviolet photodetection [17–19]. Zakutayev *et al.* reported that $ZnCo_2O_4$ is a unique material that has large work functions in the range of 5.6–5.9 eV [20], comparable to that of platinum (5.12–5.93 eV) [21]. Low-cost large work-function materials are highly desirable in optoelectronic devices. Similar to Co_3O_4, many discrepancies exist in the literature regarding the electronic structure of $ZnCo_2O_4$ [22,23]. Kim *et al.* have reported that $ZnCo_2O_4$ exhibits a bandgap of 2.63 eV, and interestingly shows both *p*-type and *n*-type conductivity depending on the oxygen partial pressure during growth of the material [24]. Samanta *et al.* found that the optical bandgap of $ZnCo_2O_4$ is of a *p-d* charge transfer nature with a value of 2.80 eV [25]. Finally, Dekkers *et al.* have reported a much different value of 2.26 eV [17]. Several theoretical studies have attempted to resolve these discrepancies in the reported bandgap of $ZnCo_2O_4$ with mixed success. Scanlon *et al.* found a small indirect bandgap of 0.57 eV using Perdew-Burke-Ernzerhof (PBE) calculation, compared to a significantly large value of 3.86 eV using hybrid exchange-correlation functional HSE06 [22]. In contrast, Amini *et al.* reported much larger values of 3.96 eV, using HSE06 calculation and 3.99 eV using GW calculation [26].

Motivated by the promise of these oxides in various device applications and to address the aforementioned fundamental questions and discrepancies in the literature, the goal of this work was to carry out a detailed investigation of the electronic, optical properties, and defect chemistry of structurally well-defined epitaxial thin films of spinel oxides. To this end, we have grown high quality epitaxial Co_3O_4, $ZnCo_2O_4$, and $CoAl_2O_4$ thin films by pulsed laser deposition (PLD). The $CoAl_2O_4$ thin films are used for the purpose of comparison, because $CoAl_2O_4$ only has Co^{2+} at T_d site, and $ZnCo_2O_4$ only has Co^{3+}*at* O_h. Co_3O_4 can be viewed as a "mixture" of $ZnCo_2O_4$ and $CoAl_2O_4$. Direct comparison of these three spinels should provide a useful perspective on the complex electronic structural evolution of Co $3d$ orbitals with different coordination and oxidization states. Compared with polycrystalline thin films in previous studies, the use of high-quality epitaxial thin films with a considerably reduced number of grain boundaries and associated defects, should reveal more intrinsic material properties. The electronic, optical, and transport properties have been investigated by a combination of x-ray photoemission spectroscopy (XPS), x-ray absorption spectroscopy (XAS), optical absorption spectra, transport measurements, and DFT calculations. We demonstrate that $ZnCo_2O_4$ exhibits a fundamental bandgap of 1.3 eV, much smaller than the generally accepted values, which range from 2.26 to 2.8 eV [17,24,25]. DFT calculations reveal that $ZnCo_2O_4$ is not a highly correlated material. We further prove that the bandgaps of Co_3O_4 and $CoAl_2O_4$ are 0.8 eV. The present results help to advance the fundamental understanding of these spinel cobaltites and provide significant guidance for the use of oxide materials in catalysis and solar energy applications.

II. EXPERIMENTAL AND COMPUTATIONAL DETAILS

Epitaxial Co_3O_4, $ZnCo_2O_4$ and $CoAl_2O_4$ thin films were grown on double-side polished (001)-oriented $MgAl_2O_4$ substrates by PLD from respective targets. Laser ablation was performed at a repetition rate of 5 Hz and an energy density of 1.0 J/cm^2 with a 248 nm KrF excimer laser. Films with thicknesses of ∼30 nm were grown at a substrate temperature of 475°C. The oxygen partial pressure during growth was 30 mTorr, unless otherwise specified. The crystal structure and epitaxial relationship in the films was determined by high-resolution x-ray diffraction (XRD) using a PANalytical four-circle diffractometer in θ-2θ scans and reciprocal space maps (RSM) mode. Optical absorption measurements were performed at room temperature using a Cary 5000 spectrophotometer in the photon energy range of 0.45–5.0 eV. Electrical resistivity measurements were performed using the van der Pauw method with Au contacts in the temperature range of 130–330 K. For Seebeck coefficient measurements, the

$5 \times 5\,\mathrm{mm}^2$ large sample was placed between the Peltier elements and temperature differences up to 8 K were applied in air at room temperature. Cross-sectional scanning transmission electron microscopy (STEM) specimens were prepared with a FEI Helios dual-beam focused ion beam/scanning electron microscope using a standard lift-out approach. A FEI Titan transmission electron microscopy with a spherical aberration corrector for the probe-forming lens operating at 300 kV was used for high-resolution STEM imaging. The surface morphologies were characterized by atomic force microscopy (AFM) (Asylum Research MFP-3D-SA) in tapping mode.

XPS measurement using a laboratory monochromatic Al Kα_1 X-ray ($h\nu = 1486.6$ eV) source was carried out at normal emission (electron take-off angle = 90° relative to the surface plane) with a SPECS PHOIBOS 150-electron energy analyzer. The total energy resolution was about 0.50 eV. The binding energy was calibrated by a Au foil in electrical contact with Co_3O_4 and $ZnCo_2O_4$ thin films, which simultaneously helped avoid charging effects during XPS measurement. The Fermi level is referenced as the zero binding energy. However, there is charging effect during measurement of $CoAl_2O_4$, because of its insulating nature. An electron flood gun was used to compensate charging effect, but meanwhile the electron flood also randomly shifts the binding energy to a higher value. To correct this shift, we align the binding energy of O 1s to be 530.0 eV, which is a commonly used method for insulating oxides in the literature [27–30]. Soft XPS and XAS measurements were performed at the Soft x-ray Spectroscopy Beamline at the Australian Synchrotron. Hard XPS (HAXPES) measurements were performed using a 6-keV photon energy at the I09 Surface and Interface Structural Analysis beamline of the Diamond Light Source, located at the Harwell Science and Innovation Campus in Oxfordshire, UK. HAXPES spectra were energy-resolved and measured using a VG Scienta EW4000 high-energy electron-energy analyzer with a 30° acceptance angle.

To understand the Co *L*-edge XAS of $ZnCo_2O_4$ and $CoAl_2O_4$, the configuration interaction (CI) calculations were carried out for a CoO_6 cluster with $3d^6$ electronic configuration under O_h symmetry and for a CoO_4 cluster with $3d^7$ electronic configuration under T_d symmetry, respectively. CI calculations taking the full multiplet effects into account show the advantages in understanding the *L*-edge excitation spectrum over the last few decades [31,32]. We consider only the three lowest energy configurations; for further details on performing the CI cluster calculations, the reader is referred to the literature [32–34]. The values of the Slater parameters representing the Coulomb and exchange interaction used in the present calculations are scaled to 80% of Slater parameters for a free ion based on the Hartree-Fock approximation due to the intra-atomic interactions inside a solid [35]. The Slater parameters obtained from Hartree-Fock approximation are ${F_{dd}}^2 = 13.412$, ${F_{dd}}^4 = 8.394$, ${F_{pd}}^2 = 7.899$, ${G_{pd}}^1 = 5.947$, ${G_{pd}}^3 = 3.384$ for the Co $3d^6$ configuration, and ${F_{dd}}^2 = 12.395$, ${F_{dd}}^4 = 7.707$, ${F_{pd}}^2 = 7.259$, ${G_{pd}}^1 = 5.394$ ${G_{pd}}^3 = 3.068$ for the Co $3d^7$ configuration.

DFT plus Hubbard U correction (U = 0, 2, and 4 eV) were carried out using the projector augmented wave method, as implemented in the Vienna *Ab Initio* Simulation Package. Projector augmented-wave pseudopotentials were used to describe the interaction between ions and electrons, the exchange-correlation potential was described by the generalized gradient approximation with the PBE parameterization. The optimization calculations were performed with a $5 \times 4 \times 5$ *k*-points sampling and a cutoff energy of 800 eV. The convergence criteria for total energies and forces were 10^{-5} eV and 10^{-5} eV/Å. The band structure along the high symmetry *k* directions in the first Brillouin zone was also calculated.

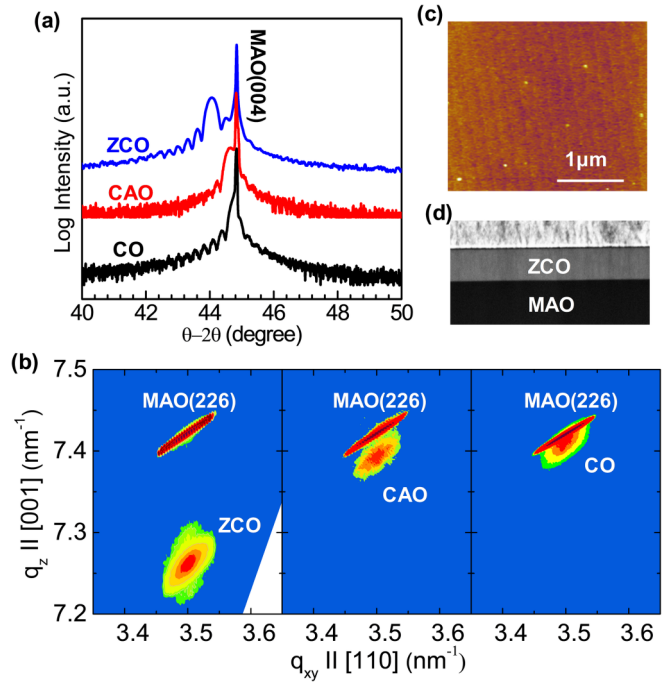

FIG. 2. (a) XRD θ-2θ scans of $ZnCo_2O_4$ (denoted as ZCO), $CoAl_2O_4$ (CAO), and Co_3O_4 (CO), showing the fringes at the vicinity of the $MgAl_2O_4$(004) reflection; (b) corresponding RSM around the $MgAl_2O_4$ (226) reflections; (c) AFM image of the $ZnCo_2O_4$ film; (d) Cross-sectional STEM image of the $ZnCo_2O_4$ film.

III. RESULTS AND DISCUSSION

A. Thin film growth

Bulk Co_3O_4, $ZnCo_2O_4$, and $CoAl_2O_4$ have very close lattice parameters of $a_{Co3O4} = 8.086$ Å, $a_{ZnCo2O4} = 8.105$ Å and $a_{CoAl2O4} = 8.095$ Å, respectively. High quality thin films can be epitaxially grown on $MgAl_2O_4$($a_{MgAl2O4} = 8.089$ Å) substrates with a small lattice mismatch (<0.2%). Figure 2(a) shows XRD θ-2θ out-of-plane scans of the three epitaxial films grown at an oxygen partial pressure (pO_2) of 30 mTorr, showing the (00*l*) reflections with well-defined Kiessig fringes close to $MgAl_2O_4$ (004) reflection, confirming the planar character of the surfaces and interfaces and the high quality of the epitaxial films. To gain additional structural information, RSMs near the (226) reflection of $MgAl_2O_4$ were measured and are shown in Fig. 2(b). The in-plane and out-of-plane lattice parameters of the films were extracted from RSMs and are shown in Table I. The in-plane lattice parameters are nearly the same as that of $MgAl_2O_4$, indicating

TABLE I. In-plane and out-of-plane lattice parameters of the films extracted from RSMs and theoretical lattice parameters, bandgaps calculated by DFT+U (U = 0, 2, and 4 eV).

				Lattice parameters (Å)			Bandgaps (eV)		
	In-plane (Å)	Out of plane (Å)	Bulk lattice (Å)	U = 0	U = 2	U = 4	U = 0	U = 2	U = 4
$ZnCo_2O_4$	8.089	8.263	8.105	8.157	8.151	8.149	0.6	1.4	2.2
Co_3O_4	8.089	8.094	8.086	8.218	8.116	8.138	0.2	1.0	1.9
$CoAl_2O_4$	8.089	8.115	8.095	8.164	8.172	8.179	0.8	2.2	3.6

all the films are coherently strained by the substrates. On the other hand, the $ZnCo_2O_4$ film shows a much larger out-of-plane lattice parameter than the bulk parameter reported in the literature, which may be caused by the compressive in-plane strain leading to an increase in the out-of-plane lattice parameter [36], and the formation of Zn vacancy during growth. AFM and cross-sectional STEM images shown in Figs. 2(c)–2(d) and Fig. S1 in the Supplemental Material [37] further confirm the atomically uniform films with well-defined surface and interfaces over a large lateral length scale.

B. Co 2*p* XPS and XAS spectra

XPS Co 2*p* and XAS spectra at the Co *L*-edge were measured in order to probe the different Co oxidization states. The Co 2*p* XPS spectra for the three oxides show a similar spin-orbital splitting of ~15.2 eV between the $2p_{3/2}$ and $2p_{1/2}$ components. The Co $2p_{3/2}$ components for $ZnCo_2O_4$, Co_3O_4, and $CoAl_2O_4$ are located at the binding energy (BE) of 779.4 eV, 779.8 eV, and 780.1 eV, respectively. It is interesting to note that the BE for Co^{2+} is higher than that of Co^{3+}, similar to that encountered in CoO and $LaCoO_3$ [38,39]. This is due to the influence of additional factors aside from oxidization state, such as change of the chemical potential and/or Madelung potential. Nevertheless, the line shape of Co $2p_{3/2}$, i.e., appearance of multiplet splitting and satellite, is more commonly used as fingerprint for discriminating different oxidization states [38–40]. For example, as shown in Fig. 3(a), the Co $2p_{3/2}$ for $ZnCo_2O_4$ exhibits a satellite at 10.6 eV higher BE and no appreciable multiplet splitting in the main peaks, in agreement with zero-spin O_h coordinated Co^{3+} (e.g., $LaCoO_3$) [39]. In contrast, the $2p_{3/2}$ for $CoAl_2O_4$ show two satellites at 5.8 and 10 eV higher BE and broader Co 2*p* main lines, resulting from unpaired 3*d* electrons at T_d Co^{2+} sites [41–43]. As expected, the Co $2p_{3/2}$ for Co_3O_4 can be viewed as a sum of spectra from $ZnCo_2O_4$ and $CoAl_2O_4$. The different oxidization states, electron occupancies and coordination environments are more notable in the Co *L*-edge XAS [(Fig. 3(b)], which probes electronic transitions from the occupied Co 2*p* core level directly into Co 3*d* unoccupied states. The line shapes depend strongly on the multiplet structures given by the atomic-like Co 2*p*-3*d* and 3*d*-3*d* Coulomb and exchange interactions, as well as by the solid state interactions including crystal fields and hybridization with O 2*p* [44]. We thus performed CI cluster calculations to simulate the Co *L*-edge XAS spectra for $ZnCo_2O_4$ using a CoO_6 cluster with $3d^6$ electron configuration under O_h symmetry, and for $CoAl_2O_4$ using a CoO_4 cluster with $3d^7$ electron configuration under T_d symmetry, respectively. Details on the calculation methods and parameters are shown in computational methods and Supplemental Material Fig. S2 and S3 [37]. Using the measured Co *L*-edge XAS as a benchmark, the obtained parameters are: $10Dq = 0.8$ eV (crystal field), $\Delta = 4$ eV (charge transfer energy), $pd\sigma = 0.5$ eV (hybridization energy), $U_{dd} = 2$ eV (Coulomb interaction) for the Co $3d^7$ ($CoAl_2O_4$) configuration, and $10Dq = 0.8$ eV, $\Delta = 3$ eV, $pd\sigma = 0.5$ eV, $U_{dd} = 2$ eV for the Co $3d^6$ ($ZnCo_2O_4$) configuration.

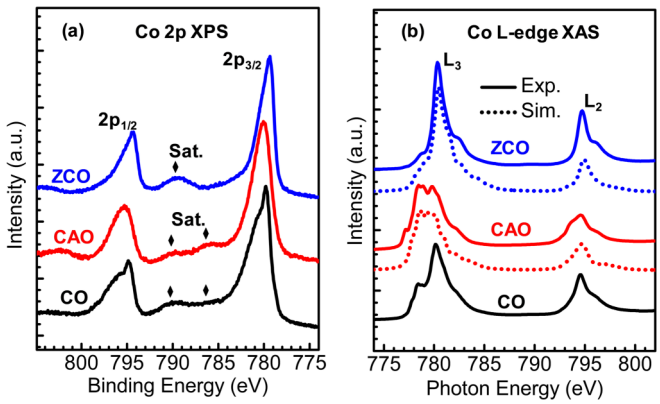

FIG. 3. (a) XPS Co 2*p* core levels of $ZnCo_2O_4$ (ZCO), $CoAl_2O_4$ (CAO) and Co_3O_4 (CO). (b) Co *L*-edge XAS (solid), and the simulated Co L-edge spectra using CI calculations for Co $3d^6$ in O_h symmetry and Co $3d^7$ in T_d symmetry.

C. Optical properties and electronic structures

Figure 4 shows the optical absorption spectra of the three films with photon energies from 0.45 to 5.0 eV. For Co_3O_4, four distinct absorption bands are clearly revealed with energies of 0.9, 1.6, 2.6, and 4.5 eV. The optical band gap of Co_3O_4 is determined to be ~0.8 eV, which is consistent with the previous reported value [10]. Similarly, a recent study of carrier dynamics of *d*-*d* excitations in Co_3O_4 has suggested the optical band gap to be 0.82 eV [11]. This optical transition originates from e_g to t_{2g} transitions at T_d-site Co^{2+} cations. This assignment is further proved by the optical spectra of $CoAl_2O_4$ which only has T_d coordinated Co^{2+}. In contrast, this transition is absent in $ZnCo_4O_4$ with purely Co^{3+} cations, and only three distinct absorption bands are clearly revealed with energies centered at around 1.3, 2.9, and 4.5 eV, respectively. As will be discussed in the following section, the transition at 1.3 eV corresponds to a *d*-*d* transition at Co^{3+}. Due to the O_h coordination of the Co^{3+} cation, the Co $3d^6$ orbital is split into three lower energy t_{2g} states being completely filled, and two higher energy e_g states being completely empty. Although this *d*-*d* transitions would be

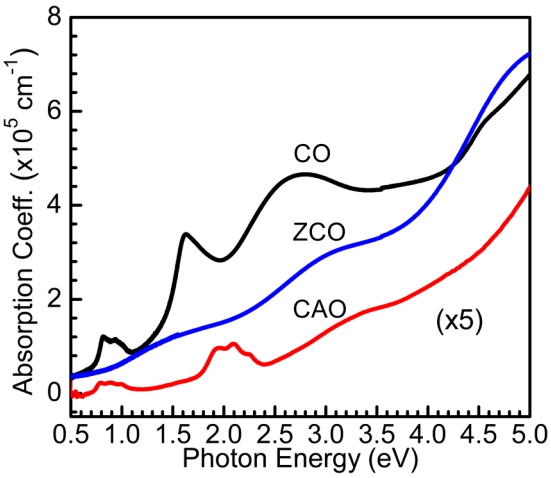

FIG. 4. Optical absorption coefficients of $ZnCo_2O_4$, $CoAl_2O_4$, and Co_3O_4 as a function of photon energy.

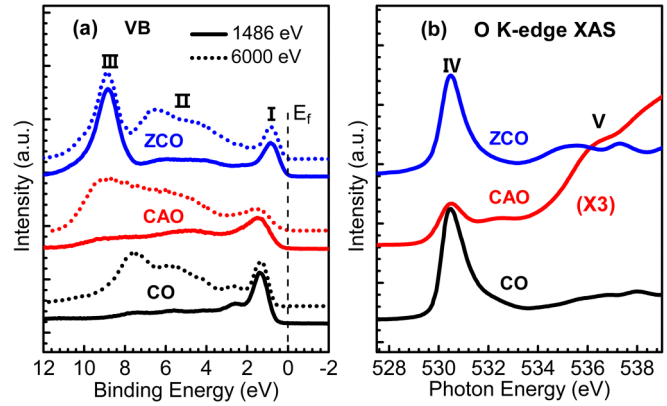

FIG. 5. (a) Valence band spectra of Co_3O_4, $ZnCo_2O_4$, and $CoAl_2O_4$ excited with photon energy of 6000 eV (dashed) and 1486.4 eV (solid); (b) corresponding O *K*-edge XAS spectra.

nominally forbidden according to the dipole selection rule, as will be discussed in details based on XPS and DFT calculations, the hybridization of Co 3*d* with O 2*p* orbitals will slightly relax the parity selection rule and result in weak light absorption. The absorption band at 2.9 eV is attributed O 2*p* to Co 3*d* excitation. These optical properties of $ZnCo_2O_4$ give rise to its higher transparency in the visible region, although the fundamental bandgap is around 1.3 eV.

A comprehensive combination of high-resolution XPS, XAS, and DFT calculations were used to elucidate the nature of electronic structure and optical transitions of Co based spinels. Figure 5(a) shows XPS valance band (VB) spectra measured at excitation photon energies of 1486.6 and 6000 eV, respectively. The VB as measured by XPS yields the occupied density of states weighted by the photoionization cross sections of the contributing orbitals. Figure 5(b) shows the O *K*-edge XAS spectra that probe the electronic transitions from the O 1*s* core level to unoccupied states with partial O 2*p* character hybridized with Co 3*d* states. The spectra can be qualitatively related to the density of states in the conduction band (CB) [45–47]. Therefore, the combination of XPS VB and O *K*-edge XAS can be used to examine the density of states (both unoccupied and occupied) near the Fermi level.

It is convenient to discuss the VB spectra shown in Fig. 5(a) in terms of three main regions, region I at BE of 0–3 eV, II at 3–7 eV, and III at 7–12 eV, and the O *K*-edge XAS spectra in Fig. 5(b) in terms of two regions, region IV at photon energy of 529–534 eV and V at 534–540 eV. For $ZnCo_2O_4$, due to the O_h coordinated Co^{3+}, the Co 3*d* is split into three lower energy t_{2g} states being completely filled by six electrons and higher energy e_g states being completely empty. Therefore, region I in the VB spectrum is assigned to the six electron occupied 3*d* t_{2g} states with some hybridization with *O* 2*p*. Correspondingly, region IV in O *K*-edge is assigned to the empty e_g states with strong hybridization with O 2*p*. The broad region V lying at higher energies consists of the empty Zn 4*s*/4*p* and Co 4*s*/4*p* derived states. Back to the VB, region II is mostly O 2*p* nonbonding derived states. $ZnCo_2O_4$ also exhibits a strong region III associated with Zn $3d^{10}$. For $CoAl_2O_4$ in which Co^{2+} is in T_d coordination, the top of VB (region I) is composed of the fully occupied e_g^4 and partly occupied t_{2g}^3 (spin-up), while the empty t_{2g}^3 (spin-down) gives rise to the region IV in O *K*-edge spectra. The assignment of the spectral features for Co_3O_4 are essentially a combination of $CoAl_2O_4$ and $ZnCo_2O_4$. The crystal field splitting values from experiments are comparable with the values as suggested by CI calculations. Interestingly, we observed that the spectral intensity of region II for the three oxides is significantly enhanced when measured using 6000-eV photon energy compared with measuring by 1486.6 eV. This suggests the contribution of Co 4*s* and Zn 4*s* orbitals to these states, because of the relatively enhanced cross sections for *s* orbitals at higher photon energy [48,49]. Recently, Panda *et al.* also reported a considerable contribution of Ni 4*s*-derived states at the VB of NiO using HAXPES, and showed that a combination of the GW and dynamical mean field theory methods is necessary for correctly describing the electronic structure of NiO [50]. In summary, the combined XPS VB and O *K*-edge measurements suggest that both the top of VB and the bottom of CB are composed mainly of Co 3*d*-orbital derived states, i.e., the bandgaps of $CoAl_2O_4$ and Co_3O_4 are largely determined by crystal field splitting of T_d coordinated Co^{2+}, and $ZnCo_2O_4$ by O_h coordinated Co^{3+}.

To gain a further understanding of XPS VB and O *K*-edge XAS spectra, we used DFT+U (U = 0, 2, and 4 eV) to calculate the electronic structures of these three oxides. Table I summarizes the calculated lattice parameters and bandgaps with different U values. For all methods, there is fairly good agreement for lattice parameters between the calculated and experimental data. However, the resultant bandgaps show a wide range variation, which is as expected in the use of DFT in modeling transition metal oxides [51]. Figure 6 shows the calculated partial density of states (PDOS) with U = 2 eV for $ZnCo_2O_4$ and Co_3O_4 and U = 0 eV for $CoAl_2O_4$ together with experimentally measured VB and O K-edge XAS spectra, and the PDOS with U = 0, 2, and 4 eV of these three oxides are shown in Supplemental Fig. S5 [37]. In order to make a direct comparison with DFT calculated DOS, we put the XPS VB and O *K*-edge XAS spectra in a common energy scale by using the band gap value obtained from optical absorption measurements. This method has been

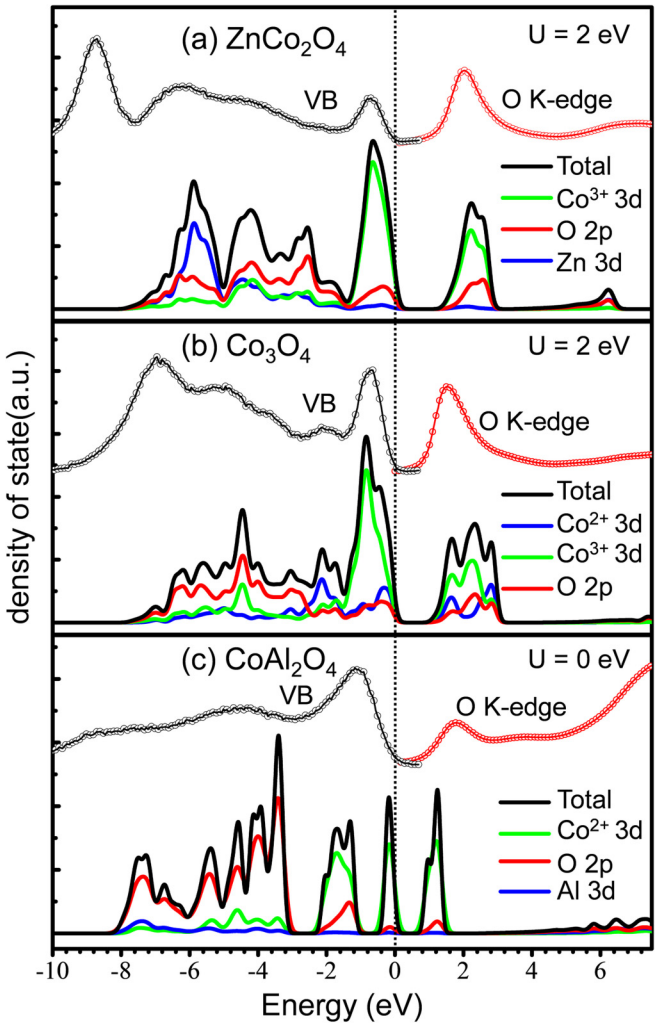

FIG. 6. PDOS of (a) $ZnCo_2O_4$, (b) Co_3O_4 and (c) $CoAl_2O_4$ calculated by DFT+U (U = 2 eV for $ZnCo_2O_4$, Co_3O_4, and U = 0 eV for $CoAl_2O_4$), together with experimental XPS VB and O K-edge spectra.

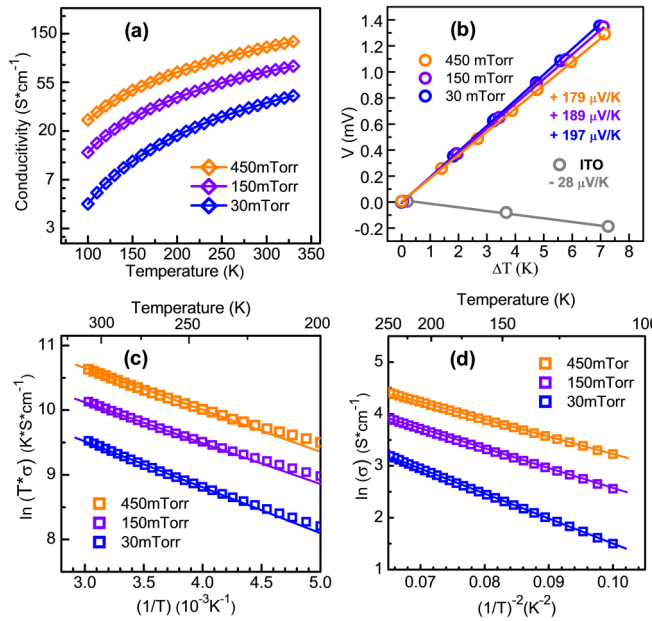

FIG. 7. Electrical and thermoelectric properties. (a) Temperature dependent conductivity of $ZnCo_2O_4$ grown at different O_2 partial pressure; (b) Seebeck measurements performed at room temperature, showing positive Seebeck coefficient (*p*-type carriers) for $ZnCo_2O_4$ films, while negative Seebeck coefficient for typical *n*-type Sn-doped In_2O_3 (ITO); (c) plots of temperature dependent conductivity data in the small polaron model using $\ln(\sigma^* T)$ vs $(1/T)$ from 330 to 200 K; (d) plots of the data to variable range hopping using $\ln(\sigma)$ vs $(1/T)^{1/2}$ from 250 to 100 K.

also widely adopted in the literature [45,52–54]. As shown in Fig. 6, the VB maximum is set as zero energy, and the leading edge of the O *K*-edge XAS at zero baseline intensity is set to be the value of the corresponding band gaps, i.e., 1.3 eV for $ZnCo_2O_4$ and 0.8 eV for $CoAl_2O_4$ and Co_3O_4**.** The validity of this method is confirmed by another commonly used method for aligning XAS with XPS VB in a common scale with reference to the Fermi energy. In this method, the XAS features are aligned above the Fermi energy by subtracting from the photon energy scale the binding energy of the relevant core levels that participate in the x-ray absorption process. To account for the influence of the core-hole final state effect, the XAS energy scale is corrected by rigidly shifting the XAS toward higher photon energies [45,55,56]. Details of the method are described in the Supplemental Material (Fig. S4 [37]). As shown in Supplemental Material Fig. S4 [37], both methods are in good agreement with each other.

Detailed analysis by comparing the band gaps in Table I and DOS in Fig. 6 and Fig. S5 [37] suggest that the results by DFT with U = 2 eV provide the best agreement with the experimentally determined band gaps, and XPS VB and O *K*-edge XAS spectra for $ZnCo_2O_4$ and Co_3O_4 DFT with U = 0 eV results in too small bandgap of 0.6 eV for $ZnCo_2O_4$ and 0.2 eV for Co_3O_4. However, calculation with a large U = 4 eV leads to much larger bandgaps of 2.2 eV for $ZnCo_2O_4$ and 1.9 eV for Co_3O_4 and 3.6 eV for $CoAl_2O_4$ and significant electronic structure distortion at the VB. For $CoAl_2O_4$, DFT with U = 0 eV provides a fairly good agreement with the experimental band gaps, although the charging effect in $CoAl_2O_4$ leads to much broader XPS VB width and poor agreement with the calculated DOS. DFT with U = 2 eV and 4 eV for $CoAl_2O_4$ results in too large band gaps (2.2 eV and 3.6 eV, respectively) and too high an energy position of unoccupied Co t_{2g} in the unoccupied DOS. The small U values for DFT are also consistent the U_{dd} = 2 eV (Coulomb interaction) used for CI calculation for XAS spectra. This suggests that $ZnCo_2O_4$, similar to Co_3O_4, is not a strongly correlated material.

D. Electrical properties and Zn vacancies as the origin of *p*-type conductivity

Co_3O_4 and $CoAl_2O_4$ thin films are not sufficiently conductive ($\sigma < 10^{-6}$ S/cm) to be measured using the van der Pauw method, whereas all the $ZnCo_2O_4$ films show high conductivity. Figure 7(a) shows the temperature dependent conductivities for three $ZnCo_2O_4$ films grown at oxygen partial pressures (pO_2) of 30, 150, and 450 mTorr. The room-temperature (RT) conductivities range from ~36 S/cm

TABLE II. Room-temperature conductivities (σ), activation energies (E_a) for small polaron hopping conduction, Seebeck coefficients (S), extracted hole concentration (p), and mobility (μ) for $ZnCo_2O_4$ films grown at different oxygen partial pressures (pO_2).

pO_2[mTorr]	σ[S cm^{-1}]	E_a[meV]	S[μV K^{-1}]	p[cm^{-3}]	μ[cm^2 V^{-1} s^{-1}]
30	36	61	197	5.1×10^{21}	0.043
150	67	55	189	5.5×10^{21}	0.076
450	111	53	179	6.0×10^{21}	0.115

for the film grown at 30 mTorr to 110 S/cm at 450 mTorr (Table II). The RT conductivities of our epitaxial films are much higher than reported values in the literatures, e.g., 5 S/cm in Ref. [20] and 21 S/cm in Ref. [57]. This is possibly due to the high crystalline quality of our epitaxial thin films. All of the films exhibit positive Seebeck coefficients [see Fig. 7(b) and Table II], confirming the *p*-type conductivity. Hall effect measurements were made to extract the carrier concentration (p) and mobility (μ), but it was not possible to obtain a reliable Hall coefficient. This is due to the low mobility of hole carriers that follow a small polaron hopping (SPH) conduction mechanism. SPH has been observed in many mixed-valence transition metal oxides such as NiO, $CuCrO_2$, and $LaCrO_3$ [45,58–60]. SPH conducts by thermally activated hopping of carriers from one site to another. The relationship between conductivity and temperature is given by $\sigma(T) = (\sigma_o/T)\exp(E_a/k_BT)$, where E_a is the activation energy for hopping and k_B is the Boltzmann constant. Figure 7(c) shows that the conductivity data fits well with a SPH model in temperature range of 220–330 K. The E_a determined from the slopes of the fit lines decreases from 61 to 53 meV. Below 220 K, the conduction data deviates from the SPH model, but fits well with variable-rang hopping that exhibits a $T^{-1/2}$ temperature dependence [Fig. 7(d)].

In order to determine p and μ, we used the Seebeck coefficient to extract of the fraction of hopping sites occupied with holes, c, based on the formula: $S(c) = (k_B/e)\ln[2(1-c)/c]$, where e is the elementary electronic charge [58]. Hole carrier concentrations p thus correspond to the activation of an adjacent Co site for hole hopping, i.e., $p = cN$, where N is the density of conducting sites, 3.0×10^{22} cm^{-3}. Based on the formulas for $S(c)$ and p, we determined the hole concentration to range from 5.1×10^{21} cm^{-3} to 6.0×10^{21} cm^{-3}. The corresponding mobilities at RT (determined from $\sigma = e\mu p$) are in the range from 0.044 to 0.116 cm^2 V^{-1} s^{-1} (see Table II). The low mobility is because of the localized nature of the VB edge formed by Co 3*d* t_{2g} orbitals. Although the *p*-type mobility is low, there are several device applications that would not be hampered by the low mobility. These include rectifiers, photodetectors, solar cells, and *n*-type junction fieldeffect transistors (*n*-JFET) [61]. In addition, it has been shown [20] that $ZnCo_2O_4$ has high work functions in the range of 5.6–5.9 eV, comparable to that of Pt with the highest work function of use in many electronic devices, but Pt is limited by its high cost. For example, in the *n*-JFET, the high hole concentration and high work function of *p*-type $ZnCo_2O_4$ would cause the depletion zone to be in the *n*-type oxide with significantly higher mobility, resulting in fast switching [62,63]. Furthermore, although $ZnCo_2O_4$ has a small bandgap, its optical excitation is dipole-forbidden. $ZnCo_2O_4$ shows reasonable transparency in the visible region. Therefore, a very thin layer (∼5–20 nm) of $ZnCo_2O_4$ can be used as hole transport layers in photovoltaic devices.

The above results show enhanced electrical conductivity in $ZnCo_2O_4$ with increasing growth partial pressure of O_2. This is also common for many other *p*-type oxides, including Cu_2O [64], NiO [65], and $CuAlO_2$ [66]. Both experimental and theoretical studies suggest that the formation of cation vacancies, e.g., Cu vacancies (V_{Cu}) in Cu_2O [64,67], and V_{Ni} in NiO [65], are the source of *p*-type conductivity. The exact origin of the *p*-type conductivity for $ZnCo_2O_4$ is still a matter of debate. Two possible defects have been proposed based on first principles calculations. Amini *et al.* using HSE0 predicted that Zn vacancies (V_{Zn}) have the lowest formation energy under oxygen-rich/Zn-poor conditions and are shallow acceptors responsible for hole carriers [26]. On the other hand, Perkins *et al.* based on generalize gradient approximation + U calculations found that Zn_{Co} antisite defects in which Zn^{2+} occupied the octahedral Co^{3+} sites are the dominant shallow acceptors for *p*-type carriers, and therefore a Zn-rich condition is required in order to increase the *p*-type conductivity [68]. It should be noted that the calculated formation energy and transition level of the defects strongly depend on the calculation methods [67]. Figure 8 shows the Zn $2p_{3/2}$ and Co $2p_{3/2}$ spectra of the three films grown at different pO_2, which indicate that the ratio of Zn relative to Co decreases with the increase of pO_2. The decrease of Zn is not unexpected, because Zn is volatile in high oxygen pressure. Supplemental Material Fig. S6 [37] shows the VB spectra and corresponding

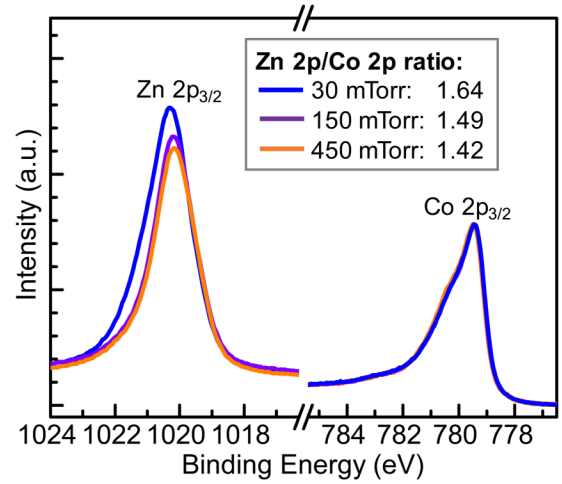

FIG. 8. Zn $2p_{3/2}$ and Co $2p_{3/2}$ spectra of the three $ZnCo_2O_4$ films grown at different pO_2; The Co $2p_{3/2}$ spectral intensity is normalized to be the same value, allowing us to directly compare the difference in Zn $2p_{3/2}$.

O 1*s* core levels of $ZnCo_2O_4$ films grown at different pO_2. Both VB and O 1*s* spectra concurrently shift 0.15 eV towards lower binding energies, because of the downward movement of the E_f by hole doping. The downward movement of Ef also parallels with the increase in RT conductivity. This suggests that the formation of V_{Zn} in higher pO_2 is mostly like the source of *p*-type conductivity, *via* $V_{zn} \rightarrow 2h^+$. The tendency to form V_{Zn} is in line with the calculation by Amini *et al.* [26] and previous experimental work by Kim *et al.* [24] that $ZnCo_2O_4$ can be both *p*-type and *n*-type doped depending on pO_2 during growth. On the other hand, *ab initio* calculations suggested that Co vacancies (V_{Co}) in Co_3O_4 are shallow acceptors as the source of *p*-type conductivity [69]. However, the formation energy of V_{Co} is much higher compared with that of V_{Zn}. To test this point, we grew Co_3O_4 thin films at $pO_2 = 450$ mTorr, and the films show much lower conductivity ($<10^{-6}$ S/cm) than $ZnCo_2O_4$ (10^2 S/cm) grown in the same conditions. Therefore, the defect chemistry of Zn at T_d sites provides flexible route to tune the electrical and optical properties of $ZnCo_2O_4$.

IV. CONCLUSIONS

In summary, using combined spectroscopic characterization and theoretical calculations, we clearly demonstrate that $ZnCo_2O_4$ has a direct fundamental bandgap of ~1.3 eV, much smaller than the generally accepted values which range from 2.26 to 2.8 eV. The VB edge of $ZnCo_2O_4$ is comprised of occupied Co 3*d* t_{2g}^6 states with some hybridization of O 2*p*/Zn 3*d* orbitals, and the CB is comprised mainly of unoccupied e_g^* states. The optical transition between the two band edges is dipole forbidden. Strong absorption occurs at photon energies above 2.6 eV, explaining the reasonable transparency of $ZnCo_2O_4$. We also show that Zn vacancies formed at high oxygen pressure are the source of a high *p*-type conductivity of $ZnCo_2O_4$ by introducing a hole state at the top of the VB, yet the hole conduction is described by small-polaron hoping model. The high *p*-type conductivity, reasonable transparency, and large work function make $ZnCo_2O_4$ a desirable *p*-type transparent semiconductor for various optoelectronic applications. Using the same method, the bandgap of Co_3O_4 is shown to be ~0.8 eV arising from the T_d coordinated Co^{2+} cations. The present results advance our fundamental understanding and provide significant guidance for the use of Co-based spinel oxides in catalysis, electronics, and solar applications. Finally, the comprehensive suite of methods we have demonstrated to resolve the electronic and optical properties of these three spinel oxides can be extended to other complex transition metal oxides, particularly in cases where the electronic structure has been insufficiently resolved.

ACKNOWLEDGMENTS

K.H.L.Z. is grateful for funding support by the Thousand Youth Talents Program of China. D.-C.Q. acknowledges the support of the Australian Research Council (Grant No. FT160100207). L.C. acknowledges the Science and Technology Research Items of Shenzhen (JCYJ20170412153325679, JCYJ20180504165650580). L.Q. is supported by the National Natural Science Foundation of China (Grant No. 11774044) and the Young 1000-talent Program. We thank Diamond Light Source for access to beamline I09 and beamline scientist Dr. P. Kumar for his kind assistance. Part of this research was undertaken on the Soft X-ray Spectroscopy beamline at the Australian Synchrotron, part of ANSTO. We acknowledge the support from beamline scientist Dr. B. Cowie at the Australian Synchrotron.

[1] Q. Zhao, Z. Yan, C. Chen, and J. Chen, Chem. Rev. **117**, 10121 (2017).
[2] X. W. Xie, Y. Li, Z. Q. Liu, M. Haruta, and W. Shen, Nature (London) **458**, 746 (2009).
[3] X. Chang, T. Wang, P. Zhang, J. Zhang, A. Li, and J. Gong, J. Am. Chem. Soc. **137**, 8356 (2015).
[4] B. Kupfer, K. Majhi, D. A. Keller, Y. Bouhadana, S. Rühle, H. N. Barad, A. Y. Anderson, and A. Zaban, Adv. Energy Mater. **5**, 1401007 (2015).
[5] K. Nagashima, T. Yanagida, K. Oka, M. Taniguchi, T. Kawai, J. S. Kim, and B. H. Park, Nano Lett. **10**, 1359 (2010).
[6] J. Beatty, T. Cheng, Y. Cao, M. S. Driver, W. A. Goddard III, and J. A. Kelber, J. Phys. Chem. Lett. **8**, 188 (2017).
[7] J. Chen, X. F. Wu, and A. Selloni, Phys. Rev. B **83**, 245204 (2011).
[8] W. Hu, X. M. Cao, and P. Hu, J. Phys. Chem. C **122**, 19593 (2018).
[9] V. Singh, M. Kosa, K. Majhi, and D. T. Major, J. Chem. Theory Comput. **11**, 64 (2015).
[10] L. Qiao, H. Y. Xiao, H. M. Meyer, J. N. Sun, C. M. Rouleau, A. A. Puretzky, D. B. Geohegan, I. N. Ivanov, M. Yoon, W. J. Weber, and M. D. Biegalski, J. Mater. Chem. C **1**, 4628 (2013).
[11] M. M. Waegele, H. Q. Doan, and T. Cuk, J. Phys. Chem. C **118**, 3426 (2014).
[12] V. L. Chevrier, S. P. Ong, R. Armiento, M. K. Y. Chan, and G. Ceder, Phys. Rev. B **82**, 075122 (2010).
[13] M. Garcia-Mota, M. Bajdich, V. Viswanathan, A. Vojvodic, A. T. Bell, and J. K. Norskov, J. Phys. Chem. C **116**, 21077 (2012).
[14] S. Selcuk and A. Selloni, J. Phys. Chem. C **119**, 9973 (2015).
[15] J. Chen and A. Selloni, J. Phys. Chem. Lett. **3**, 2808 (2012).
[16] G. Fu, X. Wen, S. Xi, Z. Chen, W. Li, J. Y. Zhang, A. Tadich, R. Wu, D. C. Qi, Y. Du, J. Cheng, and K. H. L. Zhang, Chem. Mater. **31**, 419 (2018).
[17] M. Dekkers, G. Rijnders, and D. H. A. Blank, Appl. Phys. Lett. **90**, 021903 (2007).
[18] K. H. L. Zhang, K. Xi, M. G. Blamire, and R. G. Egdell, J. Phys.: Condens. Matter **28**, 383002 (2016).
[19] F. L. Schein, M. Winter, T. Bontgen, H. von Wenckstern, and M. Grundmann, Appl. Phys. Lett. **104**, 022104 (2014).
[20] A. Zakutayev, T. R. Paudel, P. F. Ndione, J. D. Perkins, S. Lany, A. Zunger, and D. S.Ginley, Phys. Rev. B **85**, 085204 (2012).
[21] W. M. Haynes, *CRC Handbook of Chemistry and Physics* (CRC, Boca Raton, FL, 2014), Sec. 12, p. 124.
[22] D. O. Scanlon and G. W. Watson, Phys. Chem. Chem. Phys. **13**, 9667 (2011).

[23] T. R. Paudel, A. Zakutayev, S. Lany, M. d'Avezac, and A. Zunger, Adv. Funct. Mater. **21**, 4493 (2011).

[24] H. J. Kim, I. C. Song, J. H. Sim, H. Kim, D. Kim, Y. E. Ihm, and W. K. Choo, J. Appl. Phys. **95**, 7387 (2004).

[25] S. Samanta, Opt. Mater. **45**, 141 (2015).

[26] M. N. Amini, H. Dixit, R. Saniz, D. Lamoen, and B. Partoens, Phys. Chem. Chem. Phys. **16**, 2588 (2014).

[27] T. Fujii, F. M. F. de Groot, G. A. Sawatzky, F. C. Voogt, T. Hibma, and K. Okada, Phys. Rev. B **59**, 3195 (1999).

[28] S. A. Chambers, L. Qiao, T. C. Droubay, T. C. Kaspar, B. W. Arey, and P. V. Sushko. Phys. Rev. Lett. **107**, 206802 (2011).

[29] C. A. Mizzi, P. Koirala, and L. D. Marks, Phys. Rev. Mater. **2**, 025001 (2018).

[30] A. Walsh, G. W. Watson, D. J. Payne, R. G. Edgell, J. H. Guo, P. A. Glans, T. Learmonth, and K. E. Smith, Phys. Rev. B **73**, 235104 (2006).

[31] G. van der Laan, C. Westra, C. Haas, and G. A. Sawatzky, Phys. Rev. B **23**, 4369 (1981).

[32] M. W. Haverkort, M. Zwierzycki, and O. K. Andersen, Phys. Rev. B **85**, 165113 (2012).

[33] M. Wu, J. C. Zheng, and H. Q. Wang, Phys. Rev. B **97**, 245138 (2018).

[34] M. Wu, H. L. Xin, J. O. Wang, X. J. Li, X. B. Yuan, H. Zeng, J. C. Zheng, and H. Q. Wang, J. Synchrotron Rad. **25**, 777 (2018).

[35] F. M. F. de Groot, J. C. Fuggle, B. T. Thole, and G. A. Sawatzky, Phys. Rev. B **42**, 5459 (1990).

[36] K. H. L. Zhang, A. Regoutz, R. G. Palgrave, D. J. Payne, R. G. Egdell, Aron Walsh, S. P. Collins, D. Wermeille, and R. A. Cowley, Phys. Rev. B **84**, 233301 (2011).

[37] See Supplemental Material at http://link.aps.org/supplemental/10.1103/PhysRevB.100.115301 for additional AFM and STEM images and XPS spectra, details regarding DFT+U, CI calculations, and putting valence-band XPS and O *K*-edge XAS spectra on a common scale.

[38] J. van Elp, J. L. Wieland, H. Eskes, P. Kuiper, G. A. Sawatzky, F. M. F. de Groot, and T. S. Turner, Phys. Rev. B **44**, 6090 (1991).

[39] F. Munakata, H. Takahashi, Y. Akimune, Y. Shichi, M. Tanimura, Y. Inoue, R. Itti, and Y. Koyama, Phys. Rev. B **56**, 979 (1997).

[40] M. A. Langell, M. D. Anderson, G. A. Carson, L. Peng, and S. Smith, Phys. Rev. B **59**, 4791 (1999).

[41] C. A. F. Vaz, D. Prabhakaran, E. I. Altman, and V. E. Henrich, Phys. Rev. B **80**, 155457 (2009).

[42] M. Oku and K. Hirokawa, J. Electron. Spectrosc. Relat. Phenom. **8**, 475 (1976).

[43] M. Oku, J. Solid State Chem. **23**, 177 (1978).

[44] H. J. Lin, Y. Y. Chin, Z. Hu, G. J. Shu, F. C. Chou, H. Ohta, K. Yoshimura, S. Hébert, A. Maignan, A. Tanaka, L. H. Tjeng, and C. T. Chen, Phys. Rev. B **81**, 115138 (2010).

[45] K. H. L. Zhang, Y. Du, P. V. Sushko, M. E. Bowden, V. Shutthanandan, S. Sallis, L. F. J. Piper, and S. A. Chambers, Phys. Rev. B **91**, 155129 (2015).

[46] F. M. F. De Groot, M. Grioni, J. C. Fuggle, J. Ghijsen, G. A. Sawatzky, and H. Petersen, Phys. Rev. B **40**, 5715 (1989).

[47] C. Tian, M. Jiang, D. Tang, L. Qiao, H. Xiao, F. E. Oropeza, J. P. Hofmann, E. J. M. Hensen, A. Tadich, W. Li, D. C. Qi, and K. H. L. Zhang, J. Mater. Chem. A **7**, 11895 (2019).

[48] K. H. L. Zhang, D. J. Payne, R. G. Palgrave, V. K. Lazarov, W. Chen, A. T. S. Wee, C. F. McConville, P. D. C. King, T. D. Veal, G. Panaccione, P. Lacovig, and R. G. Egdell, Chem. Mater. **21**, 4353 (2009).

[49] D. W. Davies, A. Walsh, J. J. Mudd, C. F. McConville, A. Regoutz, J. M. Kahk, D. J. Payne, V. R. Dhanak, D. Hesp, K. Pussi, T.-L. Lee, R. G. Egdell, and K. H. L. Zhang, J. Phys. Chem. C **123**, 1700 (2019).

[50] S. K. Panda, B. Pal, S. Mandal, M. Gorgoi, S. Das, I. Sarkar, W. Drube, W. Sun, I. Di Marco, A. Lindblad, P. Thunström, A. Delin, O. Karis, Y. O. Kvashnin, M. van Schilfgaarde, O. Eriksson, and D. D. Sarma, Phys. Rev. B **93**, 235138 (2016).

[51] E. A. Carter, Science **321**, 800 (2008).

[52] K. Horiba, A. Chikamatsu, H. Kumigashira, M. Oshima, N. Nakagawa, M. Lippmaa, K. Ono, M. Kawasaki, and H. Koinuma, Phys. Rev. B **71**, 155420 (2005).

[53] H. Wadati, D. Kobayashi, H. Kumigashira, K. Okazaki, T. Mizokawa, A. Fujimori, K. Horiba, M. Oshima, N. Hamada, M. Lippmaa, M. Kawasaki, and H. Koinuma, Phys. Rev. B **71**, 035108 (2005).

[54] L. Wang, Y. Du, P. V. Sushko, M. E. Bowden, K. A. Stoerzinger, S. M. Heald, M. D. Scafetta, T. C. Kaspar, and S. A. Chambers, Phys. Rev. Mater **3**, 025401 (2019).

[55] A. R. H. Preston, B. J. Ruck, L. F. J. Piper, A. DeMasi, K. E. Smith, A. Schleife, F. Fuchs, F. Bechstedt, J. Chai, and S. M. Durbin, Phys. Rev. B **78**, 155114 (2008).

[56] S. Sallis, L. F. J. Piper, J. Francis, J. Tate, H. Hiramatsu, T. Kamiya, and H. Hosono, Phys. Rev. B **85**, 085207 (2012).

[57] S. Kim, J. A. Cianfrone, P. Sadik, K. W. Kim, M. Ivill, and D. P. Norton, J. Appl. Phys. **107**, 103538 (2010).

[58] J. Y. Zhang, W. Li, R. L. Z. Hoye, J. L. MacManus-Driscoll, M. Budde, O. Bierwagen, L. Wang, Y. Du, M. J. Wahila, L. F. J. Piper, T. L. Lee, H. J. Edwards, V. R. Dhanak, and K. H. L. Zhang, J. Mater. Chem. C **6**, 2275 (2018).

[59] K. H. L. Zhang, Y. Du, A. Papadogianni, O. Bierwagen, S. Sallis, L. F. J. Piper, M. E. Bowden, V. Shutthanandan, P. V. Sushko, and S. A. Chambers, Adv. Mater. **27**, 5191 (2015).

[60] L. Farrell, K. Fleischer, D. Caffrey, D. Mullarkey, E. Norton, and I. V. Shvets, Phys. Rev. B **91**, 125202 (2015).

[61] X. Yu, T. J. Marks, and A. Facchetti, Nat. Mater. **15**, 383 (2016).

[62] K. H. L. Zhang, R. Wu, F. Tang, W. Li, F. E. Oropeza, L. Qiao, V. K. Lazarov, Y. Du, D. J. Payne, J. L. MacManus-Driscoll, and M. G. Blamire, ACS Appl. Mater. Interfaces **9**, 26549 (2017).

[63] J. Y. Zhang, S. Han, W. Luo, S. Xiang, J. Zou, F. E. Oropeza, M. Gu, and K. H. L. Zhang, Appl. Phys. Lett. **112**, 171605 (2018).

[64] D. O. Scanlon, B. J. Morgan, G. W. Watson, and A. Walsh, Phys. Rev. Lett. **103**, 096405 (2009).

[65] J. A. Dawson, Y. Guo, and J. Robertson, Appl. Phys. Lett. **107**, 122110 (2015).

[66] D. O. Scanlon and G. W. Watson, J. Phys. Chem. Lett. **1**, 3195 (2010).

[67] D. O. Scanlon, B. J. Morgan, and G. W. Watson, J. Chem. Phys. **131**, 124703 (2009).

[68] J. D. Perkins, T. R. Paudel, A. Zakutayev, P. F. Ndione, P. A. Parilla, D. L. Young, S. Lany, D. S. Ginley, A. Zunger, N. H. Perry, Y. Tang, M. Grayson, T. O. Mason, J. S. Bettinger, Y. Shi, and M. F. Toney, Phys. Rev. B **84**, 205207 (2011).

[69] S. B. Cho, E. S. Sim, and Y. C. Chung, J. Eur. Ceram. Soc. **38**, 629 (2018).